Ultrastructure of the axonal periodic scaffold reveals a braid-like organization of actin rings

Stéphane Vassilopoulos[1]*, Solène Gibaud[2], Angélique Jimenez[2], Ghislaine Caillol[2], Christophe Leterrier[2]*

1. Sorbonne Université, INSERM, Institute of Myology, Centre of Research in Myology, UMRS 974, Paris, France.

2. Aix Marseille Université, CNRS, INP UMR7051, NeuroCyto, Marseille, France.

* corresponding authors: s.vassilopoulos@institut-myologie.org, christophe.leterrier@univ-amu.fr

Abstract

Recent super-resolution microscopy studies have unveiled a periodic scaffold of actin rings regularly spaced by spectrins under the plasma membrane of axons. However, ultrastructural details are unknown, limiting a molecular and mechanistic understanding of these enigmatic structures. Here, we combine platinum-replica electron and optical super-resolution microscopy to investigate the cortical cytoskeleton of axons at the ultrastructural level. We resolve actin rings as braids made of two long, intertwined actin filaments connected by a dense mesh of aligned spectrins. This molecular arrangement contrasts with the currently assumed model of actin rings made of short, capped actin filaments. We propose that braided rings explain the stability of the actin-spectrin scaffold and ultimately help preserving the axon integrity.

Neurons develop an intricate axonal arborization to ensure the proper flow and processing of information. This extraordinary architecture is built and maintained by a unique organization of the axonal cytoskeleton (Leterrier et al., 2017; Tas and Kapitein, 2018). Pioneering electron microscopy (EM) studies have revealed parallel arrays of microtubules within axons that support vesicular transport over long distances (Peters et al., 1991). Only recently has optical super-resolution microscopy been able to unveil striking actin assemblies within axons (Papandréou and Leterrier, 2018; Sigal et al., 2018): the axon is lined by a membrane-associated periodic scaffold (MPS) composed of circumferential actin rings spaced every ~185 nm by tetramers of spectrins (D'Este et al., 2015; Leterrier et al., 2015; Xu et al., 2013; Zhong et al., 2014). A molecular and mechanistic understanding of actin rings and the MPS is still lacking, as EM has not yet visualized this assembly despite its presence in virtually all neurons (D'Este et al., 2016; Dubey et al., 2018; He et al., 2016; Unsain et al., 2018b). We thus set out to investigate the ultrastructure of the axonal actin-spectrin scaffold, performing EM observation of the MPS and combining it with optical super-resolution microscopy to reveal its molecular architecture.

To obtain three-dimensional views of the axonal cortical cytoskeleton in a close to native state, without the need for detergent extraction or sectioning (Jones et al., 2014; Schrod et al., 2018), we mechanically unroofed cultured hippocampal neurons using ultrasound (Heuser, 2000). We first verified that the periodic organization of the MPS was still detected along the axon of unroofed neurons by super-resolution fluorescence microscopy based on single-molecule localization (SMLM). Staining of unroofed cultures without permeabilization highlighted the unroofed neurons with accessible ventral membrane (Fig. 1A). In unroofed proximal axons, we detected ~180 nm periodic rings for actin (Fig 1B). A similar ~190 nm periodic pattern was also obtained when labeling the carboxyterminus of ß4-spectrin along the axon initial segment (Fig. 1C) and ß2-spectrin along the more distal axon (Fig. 1D), or when combining antibodies against axonal spectrins (α2, ß2 and ß4, Fig. 1E) (Galiano et al., 2012). We measured no difference with non-unroofed, permeabilized neurons (Fig S1A-G) after quantification of the MPS spacing and periodicity using autocorrelation measurements from SMLM images, except a more marked periodicity of actin along the AIS as unroofing removed the intra-axonal actin patches (Watanabe et al., 2012).

We then imaged unroofed neurons by transmission EM of metal replicas (Heuser and Kirschner, 1980). To identify the axonal process stemming from unroofed cell bodies, we located the characteristic fascicles of AIS microtubules (yellow, Fig. 1I) (Leterrier, 2018). High-magnification views of the axonal membrane-associated cytoskeleton revealed the presence of long, parallel actin filaments, oriented perpendicular to the axis of the axon and to microtubules, and often regularly spaced by ~200 nm (magenta, Fig 1J-K, Fig. S1H, Movies S1-S3). These structures resembled braids made of two ~10 nm-diameter individual actin filaments (metal coating included). Their average spacing of 184 ± 4 nm (Fig 1L), and their presence only along the axon (Fig. 1M) strongly suggest that these braids are the periodic actin rings observed by SMLM.

To show that these braids were indeed parts of actin rings, we labeled axonal actin for platinum-replica EM (PREM) using two complementary methods. First, we used phalloidin-Alexa Fluor 488 staining followed by immunogold labeling (Jones et al., 2014) and observed numerous gold beads decorating the actin braids (Fig. 2A). Second, we used myosin subfragment 1 (S1) to decorate actin into a ropelike double helix (Heuser and Kirschner, 1980). Myosin S1 extensively decorated the actin braids (Fig. 2B) and was able to protect them during fixation and processing, as their average observable length went from 0.68 ± 0.04 µm to 1.13 ± 0.04 µm (Fig. 2C). High-magnification views of individual actin braids confirmed that braids are most often composed of two long (> 0.5 µm) intertwined actin filaments (Fig. 2D-F). This organization of actin as braids of long, unbranched filaments is to our knowledge unique (Blanchoin et al., 2014) and contrasts with the currently assumed view that axonal actin rings made of short, capped and bundled actin fil-

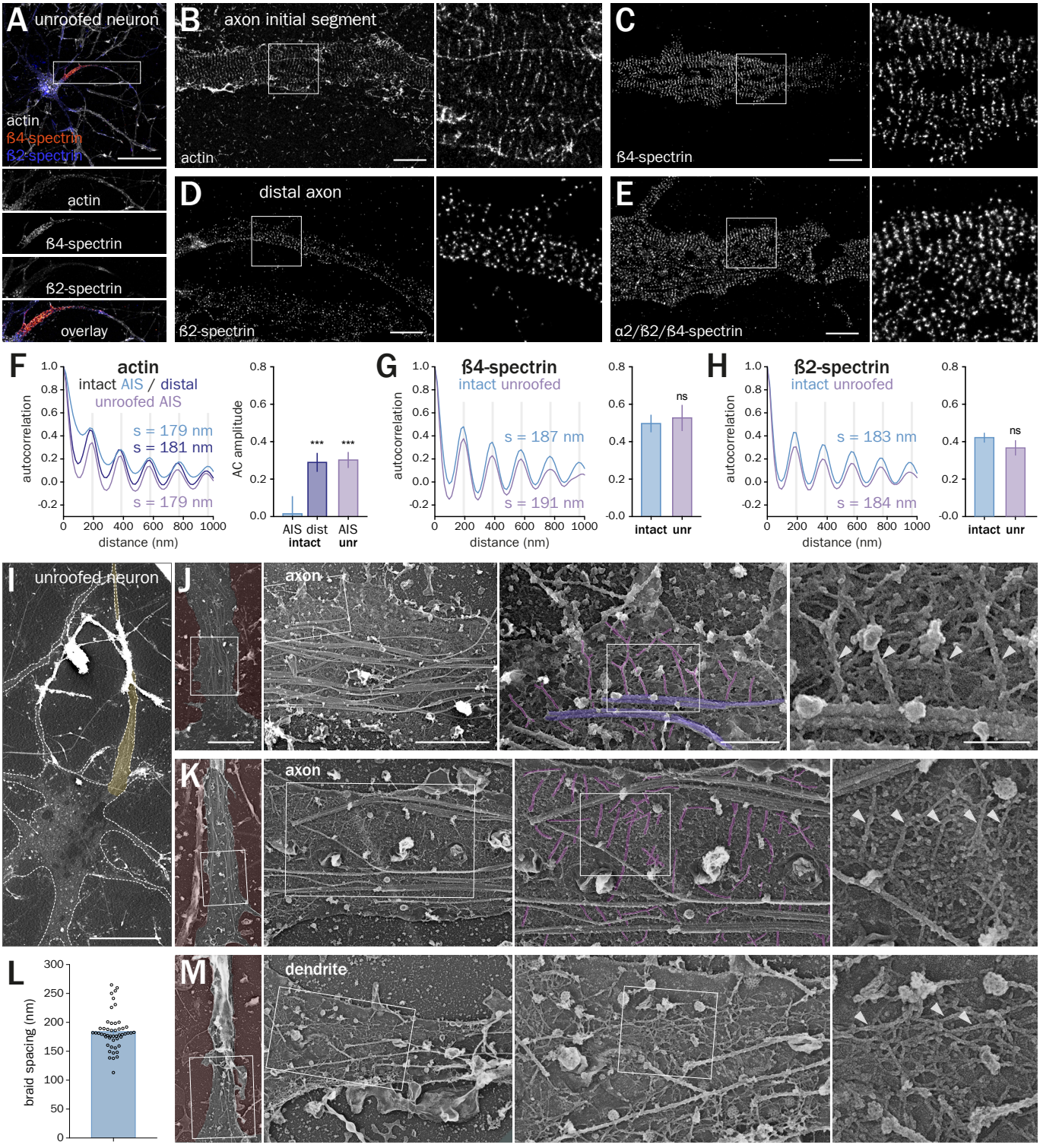

Figure 1. The actin-spectrin MPS is conserved in unroofed axons and visible by PREM.
(A) Epifluorescence image of an unroofed neuron labeled for actin (gray), ß4-spectrin (orange) and ß2-spectrin (blue). **(B-E)** SMLM images showing the periodic pattern of actin (B), ß2-spectrin (C), ß4-spectrin (D) and α2/ß2/ß4-spectrin (E) along unroofed axons. **(F-H)** Left, autocorrelation curve of the labeling for actin (F), ß4-spectrin (G), or ß2-spectrin (H). Spacing (s) is indicated. Right, measurement of corresponding the autocorrelation amplitude. **(I)** Low-magnification PREM view of an unroofed neuron and its axon (yellow). **(J-K)** PREM views of an unroofed axon showing the regularly spaced braids (magenta, arrowheads) perpendicular to microtubule fascicles (blue). **(L)** Distance between regularly-spaced actin braids in axons measured on PREM views. **(M)** PREM view of an unroofed dendrite from the same neuron shown in (K) containing mostly longitudinal actin filaments (arrowheads). Scale bars 40 µm (A), 2 µm (B-E), 20 µm (I), 5, 2, 0.5 and 0.2 µm (J-K & M, left to right).

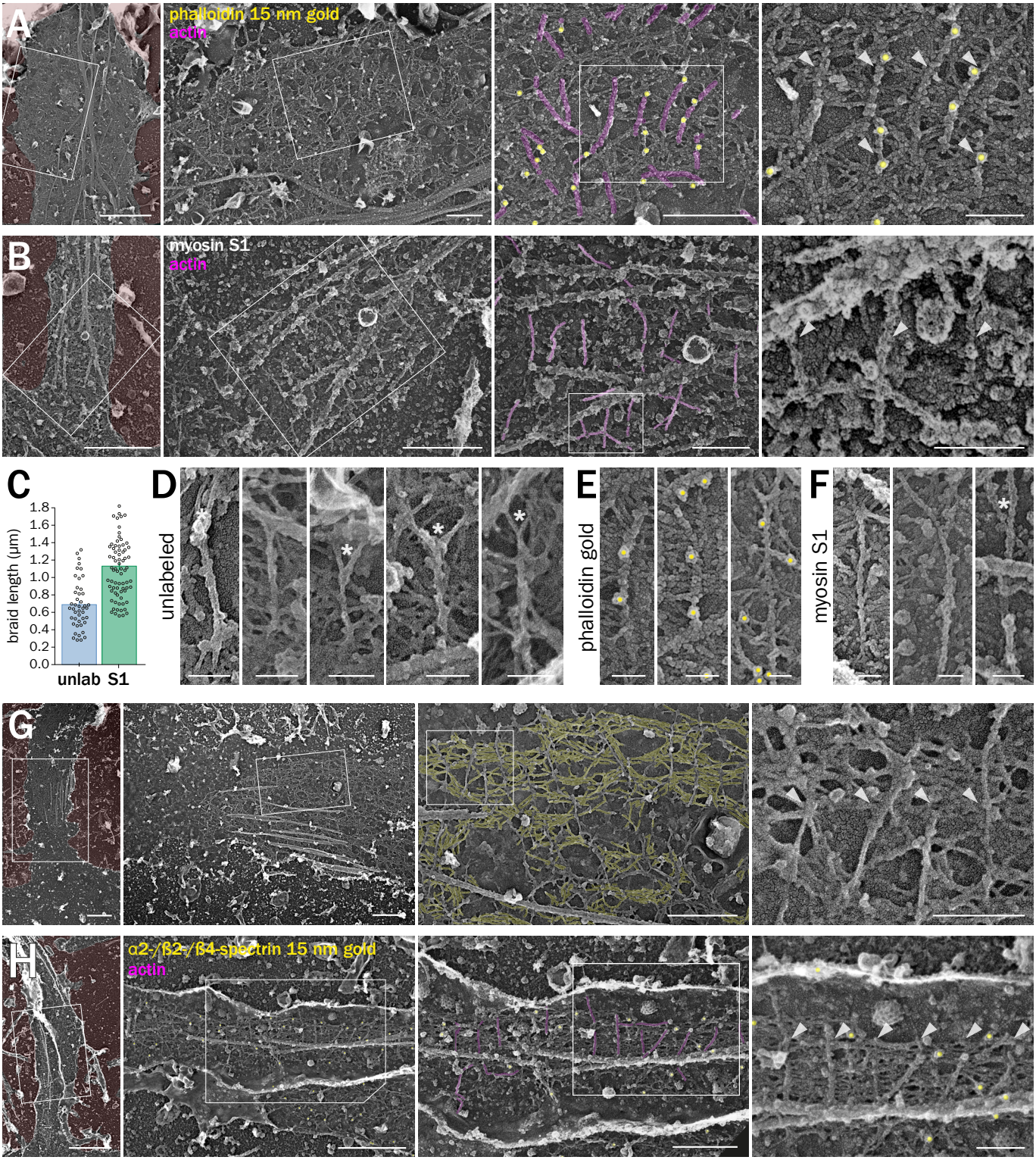

Figure 2. Actin rings are braids of long filaments connected by a spectrin mesh.
(A) PREM views of axonal actin braids (magenta, arrowheads) labeled with fluorescent phalloidin and immunogold detection of the fluorophore (15 nm gold beads, pseudo-colored yellow). **(B)** PREM views of myosin S1-treated axonal actin braids (magenta, arrowheads). **(C)** Length of the actin braids measured on PREM views in unlabeled (unlab) and myosin S1-labeled (S1) axons. **(D-F)** High-magnification views of individual unlabeled (D), immunogold-labeled (E) or myosin S1-treated (F) actin braids showing Y bifurcations (asterisks). **(G)** PREM views of unroofed axons showing the mesh (yellow) connecting actin braids. **(H)** PREM views of unroofed axons simultaneously immunogold-labeled (yellow) for α2/ß2/ß4-spectrin between actin braids (magenta, arrowheads). Scale bars 2 µm, 1, 0.5, 0.2 µm (A-B, G-H, left to right), 0.1 µm (D-F).

aments (Leite et al., 2016; Xu et al., 2013). The filaments often separate at the visible extremity of a braid, bifurcating to form a Y shape (Fig. 2D-E). This could result from the unwinding of a ring broken into braids during the unroofing and fixation procedure, as it is rarer along the myosin S1-protected braids (Fig. 2F), or may hint at the incorporation mechanism of individual actin filaments into rings.

Between actin rings, the periodic organization of spectrins implies that 190-nm long spectrin tetramers connect two adjacent rings (Fig. S1F-G) (Bennett et al., 1982; Xu et al., 2013). On our PREM images, actin braids are connected by a dense mesh of rods aligned perpendicular to the braids (yellow, Fig. 2G, Movie S4). To identify the components of this mesh, we used immunogold labeling against ß4- and ß2-spectrin. Gold beads decorated the mesh filaments in-between actin braids, although the immunolabeling efficiency was low (Fig. S2A-B). To better detect spectrins and confirm that they form the connecting mesh, we used a triple immunogold labeling of α2-, ß2- and ß4-spectrin. This resulted in a larger number of gold beads decorating the submembrane mesh, often half-way between the actin braids (Fig. 2H). Overall, the labeling experiments demonstrate that PREM resolves axonal actin rings made from pairs of long, intertwined filaments, and reveal the dense alignment of spectrins that connect these rings to form the axonal MPS.

To further connect actin rings seen by SMLM and actin braids seen by PREM, we assessed the effect of drugs that potently target actin assemblies. Due to the reported stability of the actin rings (Abouelezz et al., 2019; Leterrier et al., 2015), we used swinholide A, a drug that inhibits actin polymerization and severs existing filaments (Spector et al., 1999). We also used cucurbitacin E, a drug that inhibits filament depolymerization, stabilizes them, and is compatible with phalloidin staining (Sörensen et al., 2012). At the diffraction-limited level, acute swinholide treatment resulted in a near disappearance, while cucurbitacin induced a marked increase, of the actin staining throughout neuronal processes, with a moderate effect on spectrins labeling (Fig. S3A-B). Using SMLM, we found that swinholide could only partially disorganize the MPS along the AIS, with a periodic appearance of the remaining actin and of ß4-spectrin (Fig. 3A-B, Fig. S3C-D), whereas in the distal axon both actin and ß2-spectrin lost their periodicity (Fig. 3C-D, Fig. S3E-F). Stabilization by cucurbitacin resulted in the presence of numerous bright longitudinal bundles and clusters along the axon, making quantification of the eventual ring stabilization difficult (Fig. 3A & 3C, Fig. S3C & S3E). Cucurbitacin did not change the ß4-spectrin pattern, but ß2-spectrin showed more consistent bands and a larger autocorrelation amplitude of the pattern (Fig. 3B & 3C, Fig. S3D & S3F) (Unsain et al., 2018a). PREM views of treated, unroofed neurons (Fig. 3E) showed that swinholide induced a disappearance of the transverse actin braids, while the spectrin mesh remained visible along the proximal axon but was partially disorganized, consistent with the SMLM results (Fig. 3F). The reinforcement of the MPS induced by cucurbitacin was visible by PREM, with the occurrence of very regular stretches of actin braids connected by a densified mesh of spectrins (Fig. 3G). In addition to the similar effect detected by SMLM and PREM, these experiments show that the stable actin braids/rings can be modulated by acute perturbations, suggesting a regulated assembly and turnover.

The braids seen by PREM are not as long and continuous along the axon as the actin rings visible in SMLM (compare Fig. 1B and 1J-K). To explain this, we performed correlative SMLM and PREM on unroofed neurons. After sonication, fixation and labeling for actin and spectrin, proximal axons were imaged by SMLM before being replicated, relocated on the EM grid and observed (Sochacki et al., 2014). The nanoscale precision provided by both techniques allows to closely register the SMLM images and PREM views. Actin rings on SMLM images (Fig. 4A) closely corresponded with the braids visible on PREM views (Fig. 4B-C, Movie S5). The rings on SMLM images show that they are present along the whole width of the axon, but PREM revealed that they are often buried within the spectrin mesh, explaining their less regular appearance on PREM views (Fig. 4C). The same strategy applied to spectrins localized the center of ß4-spectrin-containing tetramers in-between actin braids on PREM views (Fig. 4E-G, Movie S6), and also located the sparse ß2-spectrin labeling of the proximal axon within the spectrin mesh (Fig. S4A-C, Movie S7).

In conclusion, we obtained the first EM images of the actin-spectrin MPS along axons and provide ultrastructural insight into its molecular organization. The simple fact that mechanical unroofing preserves the submembrane assemblies better than detergent extraction suggests that their interaction with the membrane is essential for their stability (Zhong et al., 2014). We show that axonal actin rings are made of a small number of long, intertwined filaments rather than by a large number of short, bundled filaments as previously hypothesized (Xu et al., 2013). This suggests that adducin associated with actin rings along distal axons (Leite et al., 2016; Xu et al., 2013) has a primary role in enhancing binding between actin and spectrins (Gardner and Bennett, 1987). Moreover, this arrangement is relevant to the observed stability of the MPS: closely apposed, intertwined filaments are likely to be resistant to severing factors such as ADF/cofilin (Michelot et al., 2007), and further stabilized by their embedding in the spectrin mesh. Rings made of long intertwined filaments are likely to be stiffer than bundled short filaments, hence could form the rigid part of a flexible and resistant scaffold when linked by elastic spectrins (Zhang et al., 2017), explaining the role of the MPS in the mechanical resistance of axons (Krieg et al., 2017). Beyond shedding light on the molecular underlaying of the MPS function, the ultrastructural insights obtained here could help understand its potential dysfunctions in neurodegenerative diseases, where the axonal integrity is often affected first (Encalada and Goldstein, 2014).

Author contributions and funding

SV: Conceptualization, formal analysis, funding acquisition, investigation, methodology, visualization, writing – review and editing. SG, AJ and GC: formal analysis, investigation. CL: Conceptualization, formal analysis, funding acquisition, investigation, methodology, visualization, software, supervision, writing – original draft, review and editing. This work has been funded

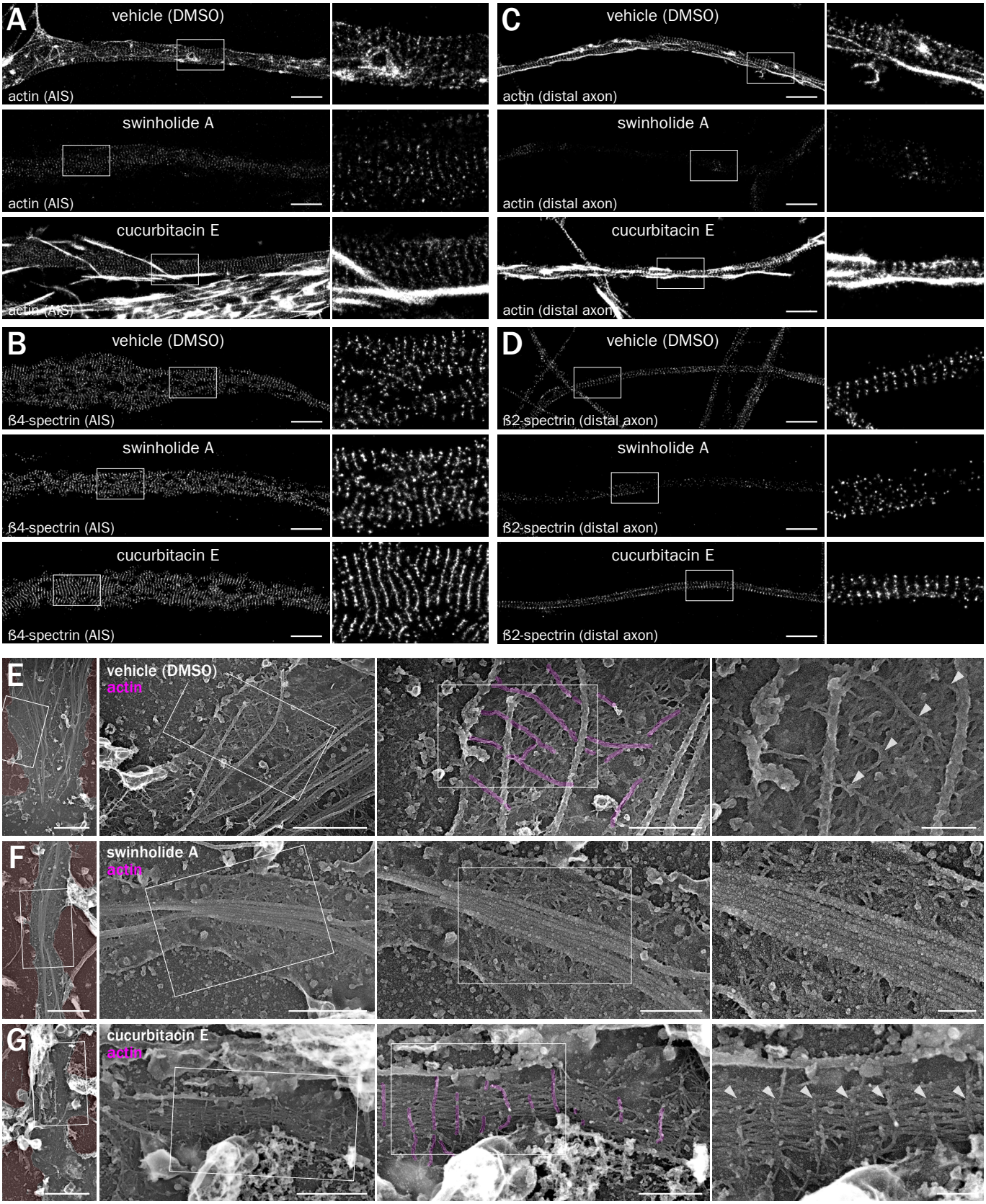

Figure 3. Actin perturbation impacts the MPS ultrastructure.
(A-D) SMLM images of AIS and distal axons treated for 3h with vehicle (DMSO 0.1%), swinholide A (100 nM) or cucurbitacin E (5 nM), labeled for actin (A & C), ß4-spectrin (B) and ß2-spectrin (D). **(E-G)** PREM views of unroofed axons from neurons treated with vehicle (E), swinholide A (F) or cucurbitacine E (G) showing the presence or absence of actin braids (magenta, arrowheads). Scale bars 2 µm (A-D), 2 µm, 1, 0.5, 0.2 µm (E-G, left to right).

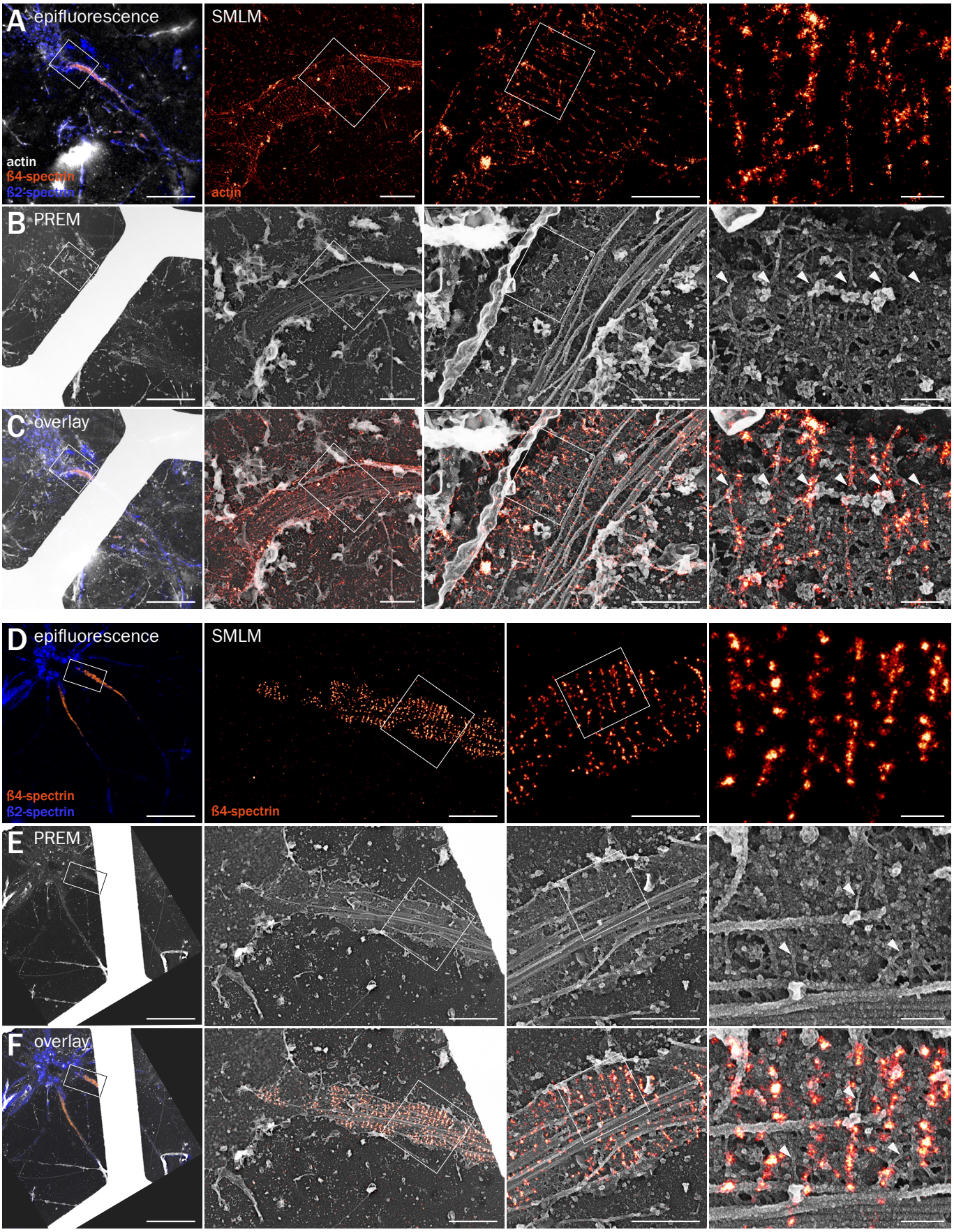

Figure 4. Correlative SMLM/PREM resolves the ultrastucture of MPS components.
(A) Left, epifluorescence image (left) of an unroofed neuron labeled for actin (gray), ß4-spectrin (orange) and ß2-spectrin (blue). Right, SMLM images of the unroofed axon labeled for actin. **(B)** Corresponding PREM views of the same unroofed neuron and axon. **(C)** Overlay of the SMLM image and PREM views showing the correspondence between actin rings in SMLM and braids in PREM (arrowheads). **(D-F)** Correlative observation of ß4-spectrin by SMLM and corresponding PREM views (actin braids are indicated by arrowheads). Scale bars 20, 2, 1, 0.2 µm (from left to right).

by the CNRS ATIP-AVENIR program (grant ATIP AO 2016 to CL); by Sorbonne Université, INSERM, Association Institut de Myologie core funding and the Agence Nationale de la Recherche (grant ANR-14-CE12-0001-01 to SV). Authors declare no competing interests.

Acknowledgements

We thank Matthew Rasband for antibody gift; Fanny Boroni-Rueda for help with neuronal cultures; the NCIS imaging facility and Nikon Instruments for SMLM equipment; the IBPS cryo-EM facility for EM equipment; Subhojit Roy, Jeanne Lainé, Marc Bitoun, Ricardo Henriques, Manuel Théry, Laurent Blanchoin, Emmanuel Nivet and the NeuroCyto team members for discussions and critical reading of the manuscript.

References

Abouelezz, A., Micinski, D., Lipponen, A., Hotulainen, P., 2019. Sub-membranous actin rings in the axon initial segment are resistant to the action of latrunculin. Biol. Chem. doi:10.1515/hsz-2019-0111

Bennett, V., Davis, J.Q., Fowler, W.E., 1982. Brain spectrin, a membrane-associated protein related in structure and function to erythrocyte spectrin. Nature 299, 126–131.

Blanchoin, L., Boujemaa-Paterski, R., Sykes, C., Plastino, J., 2014. Actin dynamics, architecture, and mechanics in cell motility. Physiological Rev 94, 235–263. doi:10.1152/physrev.00018.2013

D'Este, E., Kamin, D., Göttfert, F., El-Hady, A., Hell, S.W., 2015. STED nanoscopy reveals the ubiquity of subcortical cytoskeleton periodicity in living neurons. Cell Rep 10, 1246–1251. doi:10.1016/j.celrep.2015.02.007

D'Este, E., Kamin, D., Velte, C., Göttfert, F., Simons, M., Hell, S.W., 2016. Subcortical cytoskeleton periodicity throughout the nervous system. Sci Rep 6, 22741. doi:10.1038/srep22741

Dubey, P., Jorgenson, K., Roy, S., 2018. Actin Assemblies in the Axon Shaft - some Open Questions. Curr. Opin. Neurobiol 51, 163–167. doi:10.1016/j.conb.2018.06.012

Encalada, S.E., Goldstein, L.S.B., 2014. Biophysical challenges to axonal transport: motor-cargo deficiencies and neurodegeneration. Annu Rev Biophys 43, 141–169. doi:10.1146/annurev-biophys-051013-022746

Galiano, M.R., Jha, S., Ho, T.S.-Y., Zhang, C., Ogawa, Y., Chang, K.-J., Stankewich, M.C., Mohler, P.J., Rasband, M.N., 2012. A distal axonal cytoskeleton forms an intra-axonal boundary that controls axon initial segment assembly. Cell 149, 1125–1139. doi:10.1016/j.cell.2012.03.039

Gardner, K., Bennett, V., 1987. Modulation of spectrin-actin assembly by erythrocyte adducin. Nature 328, 359–362. doi:10.1038/328359a0

He, J., Zhou, R., Wu, Z., Carrasco, M.A., Kurshan, P.T., Farley, J.E., Simon, D.J., Wang, G., Han, B., Hao, J., Heller, E., Freeman, M.R., Shen, K., Maniatis, T., Tessier-Lavigne, M., Zhuang, X., 2016. Prevalent presence of periodic actin-spectrin-based membrane skeleton in a broad range of neuronal cell types and animal species. Proc. Natl. Acad. Sci. U.S.A 113, 6029–6034. doi:10.1073/pnas.1605707113

Heuser, J., 2000. The Production of "Cell Cortices" for Light and Electron Microscopy. Traffic 1, 545–552. doi:10.1034/j.1600-0854.2000.010704.x

Heuser, J.E., Kirschner, M.W., 1980. Filament organization revealed in platinum replicas of freeze-dried cytoskeletons. J. Cell Biol. 86, 212–234.

Jones, S.L., Korobova, F., Svitkina, T., 2014. Axon initial segment cytoskeleton comprises a multiprotein submembranous coat containing sparse actin filaments. J. Cell Biol. 205, 67–81. doi:10.1083/jcb.201401045

Kaech, S., Banker, G.A., 2006. Culturing hippocampal neurons. Nat. Protoc 1, 2406–2415.

Krieg, M., Stühmer, J., Cueva, J.G., Fetter, R., Spliker, K.A., Cremers, D., Shen, K., Dunn, A.R., Goodman, M.B., 2017. Genetic defects in β-spectrin and tau sensitize C. elegans axons to movement-induced damage via torque-tension coupling. Elife 6, 1187. doi:10.7554/eLife.20172

Leite, S.C., Sampaio, P., Sousa, V.F., Nogueira-Rodrigues, J., Pinto-Costa, R., Peters, L.L., Brites, P., Sousa, M.M., 2016. The Actin-Binding Protein α-Adducin Is Required for Maintaining Axon Diameter. Cell Rep 15, 490–498. doi:10.1016/j.celrep.2016.03.047

Leterrier, C., 2018. The Axon Initial Segment: An Updated Viewpoint. J Neurosci 38, 2135–2145. doi:10.1523/JNEUROSCI.1922-17.2018

Leterrier, C., Dubey, P., Roy, S., 2017. The nano-architecture of the axonal cytoskeleton. Nat. Rev. Neurosci 18, 713–726. doi:10.1038/nrn.2017.129

Leterrier, C., Potier, J., Caillol, G., Debarnot, C., Rueda-Boroni, F., Dargent, B., 2015. Nanoscale Architecture of the Axon Initial Segment Reveals an Organized and Robust Scaffold. Cell Rep 13, 2781–2793. doi:10.1016/j.celrep.2015.11.051

Michelot, A., Berro, J., Guérin, C., Boujemaa-Paterski, R., Staiger, C.J., Martiel, J.-L., Blanchoin, L., 2007. Actin-filament stochastic dynamics mediated by ADF/cofilin. Curr. Biol. 17, 825–833. doi:10.1016/j.cub.2007.04.037

Papandréou, M.-J., Leterrier, C., 2018. The functional architecture of axonal actin. Mol. Cell. Neurosci 91, 151–159. doi:10.1016/j.mcn.2018.05.003

Peters, A., Palay, S.L., Webster, H.D., 1991. The fine structure of the nervous system. Oxford University Press, USA.

Schrod, N., Vanhecke, D., Laugks, U., Stein, V., Fukuda, Y., Schaffer, M., Baumeister, W., Lucic, V., 2018. Pleomorphic linkers as ubiquitous structural organizers of vesicles in axons. PLoS ONE 13, e0197886. doi:10.1371/journal.pone.0197886

Sigal, Y.M., Zhou, R., Zhuang, X., 2018. Visualizing and discovering cellular structures with super-resolution microscopy. Science 361, 880–887. doi:10.1126/science.aau1044

Sochacki, K.A., Shtengel, G., van Engelenburg, S.B., Hess, H.F., Taraska, J.W., 2014. Correlative super-resolution fluorescence and metal-replica transmission electron microscopy. Nat. Methods 11, 305–308. doi:10.1038/nmeth.2816

Sörensen, P.M., Iacob, R.E., Fritzsche, M., Engen, J.R., Brieher, W.M., Charras, G., Eggert, U.S., 2012. The natural product cucurbitacin E inhibits depolymerization of actin filaments. ACS Chem. Biol. 7, 1502–1508. doi:10.1021/cb300254s

Spector, I., Braet, F., Shochet, N.R., Bubb, M.R., 1999. New anti-actin drugs in the study of the organization and function of the actin cytoskeleton. Microsc. Res. Tech. 47, 18–37. doi:10.1002/(SICI)1097-0029(19991001)47:1<18::AID-JEMT3>3.0.CO;2-E

Tas, R.P., Kapitein, L.C., 2018. Exploring cytoskeletal diversity in neurons. Science 361, 231–232. doi:10.1126/science.aat5992

Unsain, N., Bordenave, M.D., Martinez, G.F., Jalil, S., Bilderling, von, C., Barabas, F.M., Masullo, L.A., Johnstone, A.D., Barker, P.A., Bisbal, M., Stefani, F.D., Cáceres, A.O., 2018a. Remodeling of the Actin/Spectrin Membrane-associated Periodic Skeleton, Growth Cone Collapse and F-Actin Decrease during Axonal Degeneration. Sci Rep 8, 3007. doi:10.1038/s41598-018-21232-0

Unsain, N., Stefani, F.D., Caceres, A., 2018b. The Actin/Spectrin Membrane-Associated Periodic Skeleton in Neurons. Front. Synaptic Neurosci. 10, 10. doi:10.3389/fnsyn.2018.00010

Watanabe, K., Al-Bassam, S., Miyazaki, Y., Wandless, T.J., Webster, P., Arnold, D.B., 2012. Networks of polarized actin filaments in the axon initial segment provide a mechanism for sorting axonal and dendritic proteins. Cell Rep 2, 1546–1553. doi:10.1016/j.celrep.2012.11.015

Xu, K., Zhong, G., Zhuang, X., 2013. Actin, spectrin, and associated proteins form a periodic cytoskeletal structure in axons. Science 339, 452–456. doi:10.1126/science.1232251

Zhang, Y., Abiraman, K., Li, H., Pierce, D.M., Tzingounis, A.V., Lykotrafitis, G., 2017. Modeling of the axon membrane skeleton structure and implications for its mechanical properties. PLoS Comput. Biol. 13, e1005407. doi:10.1371/journal.pcbi.1005407

Zhong, G., He, J., Zhou, R., Lorenzo, D., Babcock, H.P., Bennett, V., Zhuang, X., 2014. Developmental mechanism of the periodic membrane skeleton in axons. Elife 3, 194. doi:10.7554/eLife.04581

Supplemental material

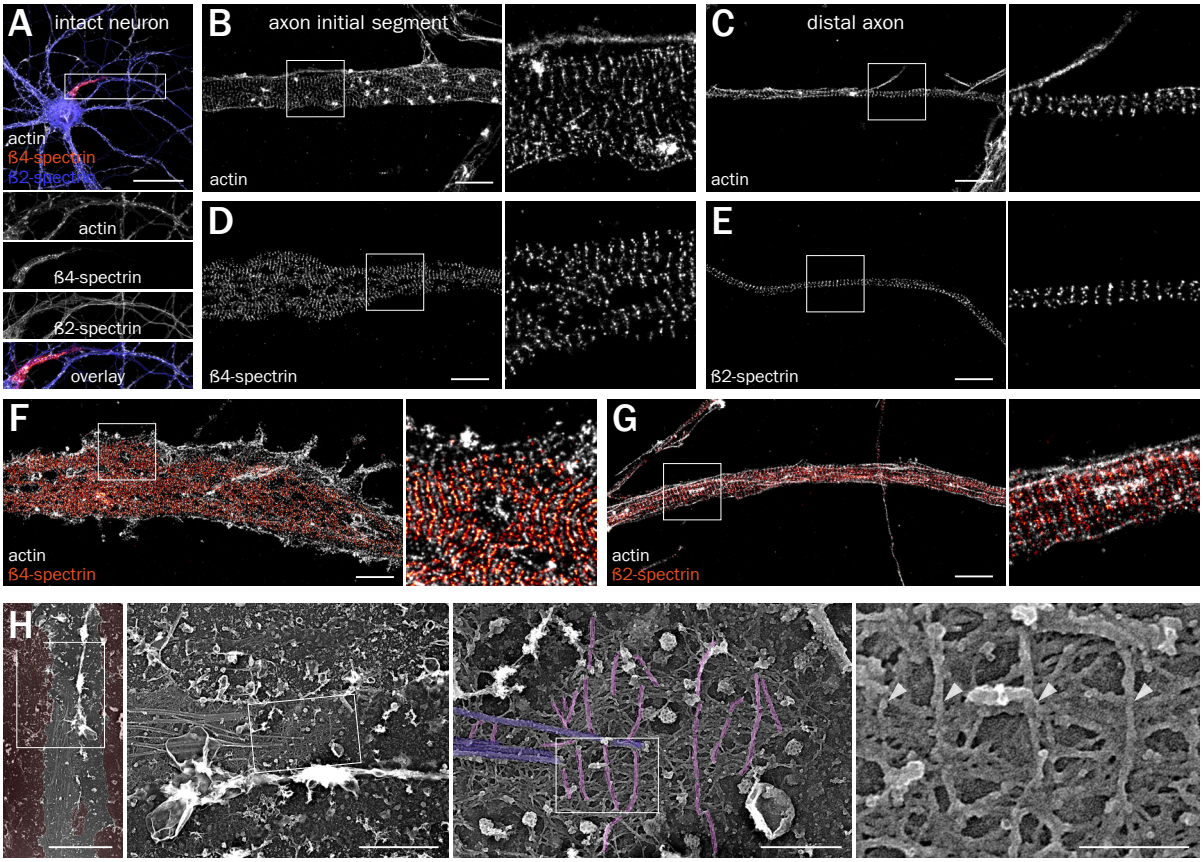

Figure S1. SMLM of the MPS along intact axons and additional PREM view of an unroofed axon.
(A) Epifluorescence image of a neuron labeled for actin (gray), ß4-spectrin (orange) and ß2-spectrin (blue). **(B-C)** SMLM images showing actin rings along the AIS (B) and the distal axon (C). **(D-E)** SMLM images showing the periodic pattern of ß4-spectrin along the AIS (D) or ß2-spectrin along the distal axon (E). **(F-G)** SMLM images showing the alternate periodic pattern of actin (gray) and ß4-spectrin along the AIS (F, orange) or ß2-spectrin along the distal axon (G, orange). **(H)** PREM view of an unroofed axon showing the regularly spaced braids (magenta, arrowheads). Scale bars 40 µm (A), 2 µm (B-G), 5, 2, 0.5 and 0.2 µm (H, left to right).

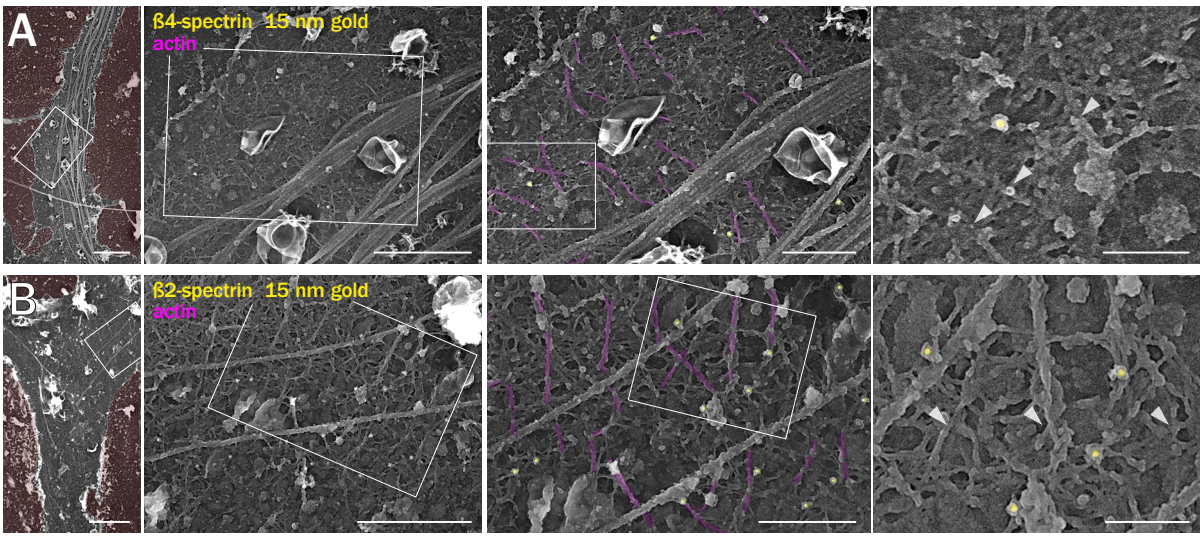

Figure S2. Immunogold labeling of the spectrin mesh.
(A-B) PREM views of unroofed axons immunogold-labeled (15 nm gold beads are pseudo-colored yellow) for ß4-spectrin (A), or ß2-spectrin (B) between actin braids (magenta, arrowheads). Scale bars 2 µm, 1, 0.5, 0.2 µm (left to right).

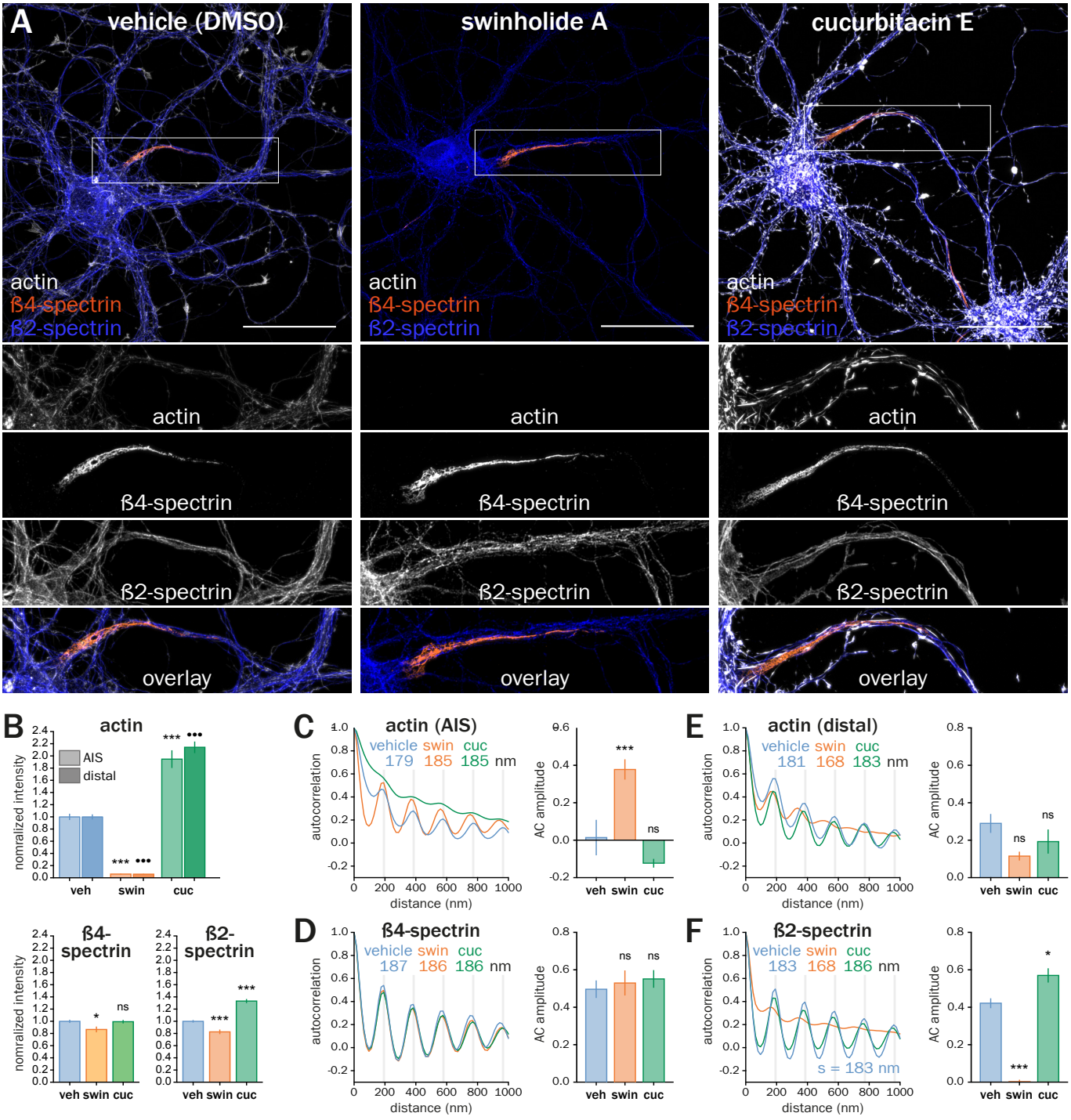

Figure S3. Epifluorescence images and quantification of drugs effects on MPS components.
(A) Epifluorescence image of neurons treated for 3h with vehicle (DMSO 0.1%), swinholide A (100 nM) or cucurbitacin E (5 nM) and labeled for actin (gray), ß4-spectrin (orange) and ß2-spectrin (blue). **(B)** Top, normalized axonal labeling intensity for actin along the AIS (light) and distal axons (dark) measured on epifluorescence images of treated neurons. Bottom, same quantification for the ß4- and ß2-spectrin labeling. **(C-F)** Left, autocorrelation curve of the labeling after drug treatment for actin along the AIS (C), ß4-spectrin (D), actin along distal axons (E), or ß2-spectrin (F). Spacing measured from the autocorrelation curve is indicated. Right, measurement of the corresponding autocorrelation amplitude for the different treatments. Scale bar, 40 µm (A).

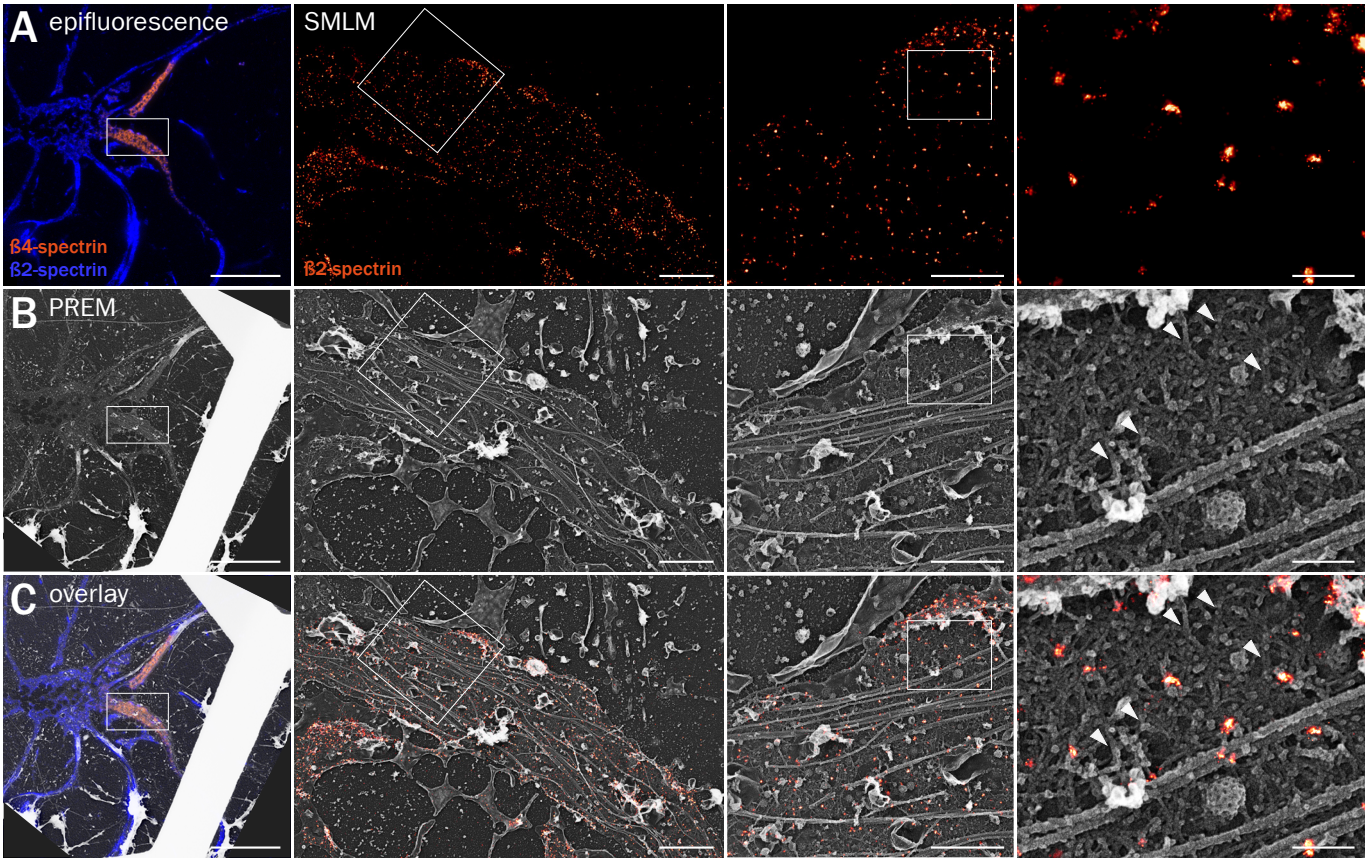

Figure S4. Correlative SMLM/PREM with ß2-spectrin labeling.
(A) Left, epifluorescence image (left) of an unroofed neuron labeled for ß4-spectrin (orange) and ß2-spectrin (blue). Right, SMLM images of the unroofed axon labeled for ß2-spectrin. **(B)** Corresponding PREM views of the same unroofed neuron and axon (actin braids, arrowheads). **(C)** Overlay of the SMLM image and PREM views. Scale bars 20, 2, 1, 0.2 µm (from left to right).

Supplemental Movies

Movie S1. Tomogram corresponding to Fig. 1J. PREM tomogram of an unroofed axon. Actin braids appear in magenta during the movie, then the spectrin mesh in yellow, and microtubules in blue.

Movie S2. Tomogram corresponding to Fig. 1K. PREM tomogram of an unroofed axon. Actin braids appear in magenta during the movie, then the spectrin mesh in yellow, and microtubules in blue.

Movie S3. Tomogram corresponding to Fig. S1H. PREM tomogram of an unroofed axon. Actin braids appear in magenta during the movie, then the spectrin mesh in yellow, and microtubules in blue.

Movie S4. Tomogram corresponding to Fig. 2G. PREM tomogram of an unroofed axon. Actin braids appear in magenta during the movie, then the spectrin mesh in yellow, and microtubules in blue.

Movie S5. Correlative PREM/SMLM for actin corresponding to Fig 4A-C. The unroofed neuron is shown with successive epifluorescence image (ß2-spectrin in green, ß4-spectrin in red, actin in blue), low-magnification PREM image (grid appears white), SMLM image (actin in orange) and high-magnification PREM image of the proximal axon. The high-magnification PREM image of the axon is then superimposed with the SMLM image (actin in orange).

Movie S6. Correlative PREM/SMLM for ß4-spectrin corresponding to Fig 4D-F. The high-magnification PREM image of the axon is superimposed with the SMLM image (ß4-spectrin in orange).

Movie S7. Correlative PREM/SMLM for ß2-spectrin corresponding to Fig S4A-C. The high-magnification PREM image of the axon is superimposed with the SMLM image (ß2-spectrin in orange).

Materials and Methods

Antibodies and reagents

Rabbit polyclonal anti ßIV-spectrin antibody (against residues 2237-2256 of human ßIV-spectrin, 1:800 dilution for immunofluorescence IF, 1:20 for immunogold IG) was a gift from Matthew Rasband (Baylor College of Medicine, Austin, TX). Mouse monoclonal anti ßII-spectrin (against residues 2101-2189 of human ßII-spectrin, 1:100 for IF, 1:20 for IG) was from BD Biosciences (#612563). Chicken anti-map2 antibody was from abcam (#ab5392, 1:1000 for IF). Rabbit polyclonal anti-Alexa Fluor 488 antibody was from Thermo Fisher (A11094, 1:20 for IG). Donkey and goat anti-rabbit and anti-mouse secondary antibodies conjugated to Alexa Fluor 488, 555 and 647 were from Life Technologies or Jackson ImmunoResearch (1:200-1:400 for IF). Donkey anti-rabbit and anti-mouse secondary antibodies conjugated to DNA PAINT handles P1 (ATACATCTA) and P3 (TCTTCATTA), respectively, were prepared according to published procedures (Schnitzbauer et al., 2017). Goat anti-rabbit and anti-mouse secondary antibodies conjugated to 15 nm gold nanobeads were from Aurion (#815011 and #815022 respectively, 1:20 for IG).

Alexa-Fluor 488 and Alexa-Fluor 647 conjugated phalloidins were from Thermo Fisher (#A12379 and #A2287 respectively), Atto488 conjugated phalloidin (#AD488-81) was from Atto-Tec. DMSO (#D2650), swinholide A (#S9810), cucurbitacine E (#PHL800-13), glutaraldehyde (#G5882) were from Sigma. Paraformaldehyde (PFA, #15714, 32% in water) was from Electron Microscopy Sciences. Myosin S1 (from rabbit skeletal fast muscle) was from Hypermol (#9310-01).

Animals and neuronal cultures

The use of Wistar rats followed the guidelines established by the European Animal Care and Use Committee (86/609/CEE) and was approved by the local ethics committee (agreement D13-055-8). Rat hippocampal neurons were cultured following the Banker method, above a feeder glia layer (Kaech and Banker, 2006). Rapidly, 12 or 18 mm-diameter round, #1.5H coverslips were affixed with paraffine dots as spacers, then treated with poly-L-lysine. Hippocampi from E18 rat pups were dissected, and homogenized by trypsin treatment followed by mechanical trituration and seeded on the coverslips at a density of 4,000-8,000 cells/cm2 for 3 hours in serum-containing plating medium. Coverslips were then transferred, cells down, to petri dishes containing confluent glia cultures conditioned in B27-supplemented Neurobasal medium and cultured in these dishes for up to 4 weeks. For this work, neurons were fixed at 13 to 17 days in vitro, a stage where they exhibit a membrane-associated periodic scaffold (MPS) along virtually all axons (Xu et al., 2013).

Cell treatments, fluorescence immunocytochemistry

Treatments were applied on neurons in their original culture medium for 3h at 37°C, 5% CO2: DMSO 0.1% (from pure DMSO), swinholide A 100 nM (from 100 µM stock in DMSO), cucurbitacin E 5 nM (from 5 µM stock in DMSO). Stock solutions were stored at -20°C.

For epifluorescence and SMLM of intact neurons, cells were fixed using 4% PFA in PEM buffer (80 mM PIPES pH 6.8, 5 mM EGTA, 2 mM $MgCl_2$) for 10 minutes at room temperature (RT). After rinses in 0.1M phosphate buffer (PB), neurons were blocked for 2-3h at RT in immunocytochemistry buffer (ICC: 0.22% gelatin, 0.1% Triton X-100 in PB), and incubated with primary antibodies diluted in ICC overnight at 4°C. After rinses in ICC, neurons were incubated with secondary antibodies diluted in ICC for 1h at RT, rinsed and incubated in fluorescent phalloidin at 0.5 µM for either 1h at RT or overnight at 4°C. Stained coverslips were kept in PB + 0.02% sodium azide at 4°C before SMLM imaging. For epifluorescence imaging, coverslips were mounted in ProLong Glass (Thermo Fisher #P36980).

Unroofing and PREM immunocytochemistry

Unroofing was performed by sonication as previously described (Heuser, 2000). Coverslips where quickly rinsed three times in Ringer+Ca (155 mM NaCl, 3 mM KCl, 3 mM NaH_2PO_4, 5 mM HEPES, 10 mM glucose, 2 mM $CaCl_2$, 1 mM $MgCl_2$, pH 7.2), then immersed ten seconds in Ringer-Ca (155 mM NaCl, 3 mM KCl, 3 mM NaH_2PO_4, 5 mM HEPES, 10 mM glucose, 3 mM EGTA, 5 mM $MgCl_2$, pH 7.2) containing 0.5 mg/mL poly-L-lysine, then quickly rinsed in Ringer-Ca then unroofed by scanning the coverslip with rapid (2-5s) sonicator pulses at the lowest deliverable power in KHMgE buffer (70 mM KCl, 30 mM HEPES, 5 mM $MgCl_2$, 3 mM EGTA, pH 7.2).

Unroofed cells were immediately fixed using fixative in KHMgE: 4% PFA for 10 minutes for epifluorescence or SMLM of fluorescence-labeled samples, 4% PFA for 45 minutes for PREM of immunogold-labeled samples, 3% PFA-1% glutaraldehyde or 2% PFA-2% glutaraldehyde for 10 to 20 minutes for PREM and correlative SMLM/PREM. Glutaraldehyde-fixed samples were subsequently quenched using 0.1% $NaBH_4$ in KHMgE for 10 minutes. Immunofluorescence labeling was performed as above, but replacing the ICC buffer with a detergent-free buffer (KHMgE, 1% BSA). Immunogold labeling was performed in the same detergent-free solution: samples were blocked for 30', incubated 1h30 with the primary antibodies diluted to 1:20, rinsed, incubated two times 20 minutes with the gold-coupled secondary antibodies, then rinsed.

Actin immunogold and myosin S1 labeling

For immunogold labeling of actin (Jones et al., 2014), unroofed neurons were fixed with 2% PFA in KHMgE, then quenched for 10 minutes in KHMgE, 100 mM glycine, 100 mM NH_4Cl. After blocking in KHMgE, 1% BSA, they were incubated with phalloidin-Alexa Fluor 488 (0.5 µM) for 45 minutes, then immunolabeled using an anti-Alexa Fluor 488 primary antibody and a gold-coupled goat anti-rabbit secondary antibody as described above for immunogold labeling.

For myosin S1 labeling, neurons were unroofed in PEM100 buffer (100 mM PIPES-KOH pH 6.9, 1 mM $MgCl_2$, 1 mM EGTA), treated with 0.25 mg/mL myosin S1 in PEM100 buffer for 30 minutes, then fixed with 2% glutaraldehyde in PEM100 buffer for 10 minutes.

Platinum-replica sample processing

Fixed samples were stored and shipped in KHMgE, 2% glutaraldehyde. Cells were further sequentially treated with 0.5% OsO_4, 1% tannic acid and 1% uranyl acetate prior to graded ethanol dehydration and hexamethyldisilazane substitution (HMDS) (Sigma). Dried samples were then rotary-shadowed with 2 nm of platinum and 5-8 nm of carbon using an ACE600 high vacuum metal coater (Leica Microsystems). The resultant platinum replica was floated off the glass with hydrofluoric acid (5%), washed several times on distilled water, and picked up on 200 mesh formvar/carbon-coated EM grids.

Epifluorescence and SMLM

Diffraction-limited images were obtained using an Axio-Observer upright microscope (Zeiss) equipped with a 40X NA 1.4 or 63X NA 1.46 objective and an Orca-Flash4.0 camera (Hamamatsu). Appropriate hard-coated filters and dichroic mirrors were used for each fluorophore. Quantifications were performed on raw, unprocessed images. An Apotome optical sectioning module (Zeiss) and post-acquisition deconvolution (Zen software, Zeiss) were used to acquire and process images used for illustration.

For single color SMLM, we used STochastic Optical Microscopy (STORM). STORM was performed on an N-STORM microscope (Nikon Instruments). Coverslips were mounted in a silicone chamber filled with STORM buffer (Smart Buffer Kit, Abbelight). The N-STORM system uses an Agilent MLC-400B laser launch with 405 nm (50 mW maximum fiber output power), 488 nm (80 mW), 561 mW (80 mW) and 647 nm (125 mW) solid-state lasers, a 100X NA 1.49 objective and an Ixon DU-897 camera (Andor). After locating a suitable neuron using low-intensity illumination, a TIRF image was acquired, followed by a STORM acquisition. 30,000-60,000 images (256x256 pixels, 15 ms exposure time) were acquired at full 647 nm laser power. Reactivation of fluorophores was performed during acquisition by increasing illumination with the 405 nm laser. When imaging actin, 30 nM phalloidin-Alexa Fluor 647 was added to the STORM buffer to mitigate actin unbinding during imaging (Jimenez et al., 2019).

For two-color SMLM (Fig. 1D-E), we used STORM in combination with DNA-PAINT (Schnitzbauer et al., 2017). Neurons were labeled using secondary antibodies coupled to a PAINT DNA handle for ß4- or ß2-spectrin (rabbit P3 or mouse P1, respectively), as well as phalloidin-Alexa Fluor 647 for actin. Imaging was done sequentially (Jimenez et al., 2019), first for actin in STORM buffer (60,000 frames at 67 Hz), then for ß4- or ß2-spectrin in PAINT buffer (0.1M phosphate buffer saline, 500 mM NaCl, 5% dextran sulfate, pH 7.2) supplemented with 0.12-0.25 nM of the corresponding PAINT imager strand coupled to Atto650 (Metabion, 40,000 frames at 33 Hz). No chromatic aberration correction was necessary as both channels were acquired using the same spectral channel, and translational shift was corrected by autocorrelation and manual refinement.

The N-STORM software (Nikon Instruments) was used for the localization of single fluorophore activations. After filtering out localizations to reject too low and too high photon counts, the list of localizations was exported as a text file. Image reconstructions were performed using the ThunderSTORM ImageJ plugin (Ovesny et al., 2014) in Fiji software (Schindelin et al., 2012). Custom scripts and macros were used to translate localization files from N-STORM to ThunderSTORM formats, as well as automate images reconstruction for whole images and detailed zooms. STORM processing scripts used in this work can be found at https://github.com/cleterrier/ChriSTORM.

Fluorescence image analysis

Quantification of the labeling intensities on epifluorescence images was done by first tracing the region of interest along a process (AIS, axon or dendrite) using the NeuronJ plugin (Meijering et al., 2004) in Fiji software. Tracings were then translated into ImageJ ROIs and the background-corrected intensities were measured for each labeled channel. Intensity measurement scripts are available at https://github.com/cleterrier/Measure_ROIs.

Quantification of the scaffold periodicity on SMLM images was performed using autocorrelation analysis (Zhong et al., 2014): if an intensity profile is periodically patterned, its autocorrelation curve will exhibit regular peaks at multiples values of the period (here 190 nm, 380 nm, 760 nm etc). The position of the first peak of the autocorrelation curve can be used to retrieve the average spacing (s), and its height estimates how marked the periodicity of the profile is. Axons were manually traced in ImageJ using polyline ROIs on 16 nm/pixel reconstructed images. The normalized autocorrelation curve of the corresponding intensity profile was calculated and plotted. The ImageJ script for generating autocorrelation curves from polyline ROIs is available at https://github.com/cleterrier/Process_Profiles. Autocorrelation curves of all tracings for a given labeling and condition were then averaged. The first non-zero peak of the averaged autocorrelation curve was fitted in Prism (Graphpad software) to estimate its position, providing the spacing value (s) and the corresponding error. The autocorrelation amplitude (height of the first peak) was estimated from the difference between the autocorrelation values at 192 nm (approximate position of the first peak) and 96 nm (approximate position of the first valley).

EM of platinum replicas

Replicas on EM grids were mounted in a eucentric side-entry goniometer stage of a transmission electron microscope operated at 80 kV (model CM120; Philips) and images were recorded with a Morada digital camera (Olympus). Images were processed in Photoshop (Adobe) to adjust brightness and contrast and presented in inverted contrast. Tomograms were made by collecting images at the tilt angles up to ±25° relative to the plane of the sample with 5° increments. Images were aligned by layering them on top of each other in Photoshop.

Correlative SMLM/PREM

For correlative SMLM/PREM, unroofed and stained samples were first imaged by epifluorescence, then a STORM image was acquired (see above). At the end of the acquisition a ob-

jective-style diamond scriber (Leica) was used to engrave a ~1 mm circle around the imaged area, and a low-magnification, 10X phase image was taken as a reference for relocation. After replica generation and prior to its release, the coated surface of each coverslip was scratched with a needle to make an EM-grid sized region of interest containing the engraved circle. Grids were imaged with low magnification EM to relocate the region that previously imaged by epifluorescence and SMLM, and high-magnification EM views were taken from the corresponding axonal region. A high-resolution SMLM reconstruction was mapped and aligned by affine transformation to the corresponding high-magnification EM view using the eC-CLEM plugin in ICY software (Paul-Gilloteaux et al., 2017).

Data representation and statistical analysis

Intensity profiles, graphs and statistical analyses were generated using Prism. On bar graphs, dots (if present) are individual measurements, bars or horizontal lines represent the mean, and vertical lines are the SEM unless otherwise specified. Significances were tested using two-tailed unpaired non-parametric t-tests (two conditions) or one-way non-parametric ANOVA followed by Tukey post-test (3 or more conditions). In all figures, significance is coded as: ns non-significant, * $p < 0.05$, ** $p < 0.01$, *** $p < 0.001$. The number of data points and experiments for quantitative results is presented in Table S1 and S2. The measurements presented in Fig. 1 are from the same pooled dataset as the control condition in Fig. 3.

Supplemental references

Heuser, J., 2000. The Production of "Cell Cortices" for Light and Electron Microscopy. Traffic 1, 545–552. doi:10.1034/j.1600-0854.2000.010704.x

Jimenez, A., Friedl, K., Leterrier, C., 2019. About samples, giving examples: optimized procedures for Single Molecule Localization Microscopy. Methods. doi:10.1016/j.ymeth.2019.05.008

Jones, S.L., Korobova, F., Svitkina, T., 2014. Axon initial segment cytoskeleton comprises a multiprotein submembranous coat containing sparse actin filaments. J. Cell Biol. 205, 67–81. doi:10.1083/jcb.201401045

Kaech, S., Banker, G.A., 2006. Culturing hippocampal neurons. Nat. Protoc 1, 2406–2415.

Meijering, E., Jacob, M., Sarria, J., Steiner, P., Hirling, H., Unser, M., 2004. Design and validation of a tool for neurite tracing and analysis in fluorescence microscopy images. Cytometry A 58A, 167–176.

Michelot, A., Berro, J., Guérin, C., Boujemaa-Paterski, R., Staiger, C.J., Martiel, J.-L., Blanchoin, L., 2007. Actin-filament stochastic dynamics mediated by ADF/cofilin. Curr. Biol. 17, 825–833. doi:10.1016/j.cub.2007.04.037

Ovesny, M., Křižek, P., Borkovec, J., Svindrych, Z., Hagen, G.M., 2014. ThunderSTORM: a comprehensive ImageJ plug-in for PALM and STORM data analysis and super-resolution imaging. Bioinformatics 30, 2389–2390. doi:10.1093/bioinformatics/btu202

Paul-Gilloteaux, P., Heiligenstein, X., Belle, M., Domart, M.-C., Larijani, B., Collinson, L., Raposo, G., Salamero, J., 2017. eC-CLEM: flexible multidimensional registration software for correlative microscopies. Nat. Methods 14, 102–103. doi:10.1038/nmeth.4170

Schindelin, J., Arganda-Carreras, I., Frise, E., Kaynig, V., Longair, M., Pietzsch, T., Preibisch, S., Rueden, C., Saalfeld, S., Schmid, B., Tinevez, J.-Y., White, D.J., Hartenstein, V., Eliceiri, K.W., Tomancak, P., Cardona, A., 2012. Fiji: an open-source platform for biological-image analysis. Nat. Methods 9, 676–682. doi:10.1038/nmeth.2019

Schnitzbauer, J., Strauss, M.T., Schlichthaerle, T., Schueder, F., Jungmann, R., 2017. Super-resolution microscopy with DNA-PAINT. Nat. Protoc 12, 1198–1228. doi:10.1038/nprot.2017.024

Xu, K., Zhong, G., Zhuang, X., 2013. Actin, spectrin, and associated proteins form a periodic cytoskeletal structure in axons. Science 339, 452–456. doi:10.1126/science.1232251

Zhong, G., He, J., Zhou, R., Lorenzo, D., Babcock, H.P., Bennett, V., Zhuang, X., 2014. Developmental mechanism of the periodic membrane skeleton in axons. Elife 3, 194. doi:10.7554/eLife.04581

		Intensity along axons from epifluorescence					Autocorrelation of axonal segments from SMLM						
		Normalized intensity		Number of data points			Spacing s (µm)		Amplitude		Number of data points		
Labeling	*Treatment*	*Mean*	*SEM*	*Tracings*	*Images*	*Indep. exp*	*Fit value*	*Error*	*Mean*	*SEM*	*Tracings*	*Images*	*Indep. exp*
actin (AIS)	vehicle	1,000	0,051	77	34	5	0,179	0,007	0,014	0,095	18	14	4
	unroofed						0,187	0,002	0,302	0,043	42	32	6
	swin	0,061	0,006	46	30	3	0,185	0,003	0,378	0,054	20	9	3
	cuc	1,948	0,146	65	24	3	0,142	0,287	-0,123	0,023	8	9	3
actin (distal)	ctrl	1,000	0,042	451	34	5	0,181	0,003	0,289	0,051	52	13	4
	swin	0,061	0,006	177	30	3	0,168	0,012	0,115	0,023	15	9	3
	cuc	2,142	0,095	283	24	3	0,183	0,004	0,192	0,064	27	9	3
ß4-spectrin	ctrl	1,000	0,026	107	56	6	0,187	0,002	0,497	0,047	43	14	3
	unroofed						0,191	0,002	0,527	0,070	16	9	2
	swin	0,867	0,047	74	52	4	0,186	0,002	0,530	0,067	25	12	2
	cuc	0,993	0,029	105	46	5	0,186	0,002	0,552	0,047	33	14	3
ß2-spectrin	ctrl	1,000	0,019	777	66	7	0,184	0,001	0,422	0,026	60	18	4
	unroofed						0,185	0,003	0,367	0,041	30	15	2
	swin	0,677	0,027	450	62	5	0,163	0,017	0,003	0,010	29	15	3
	cuc	1,285	0,031	502	56	5	0,188	0,001	0,570	0,038	31	11	2

Table S1. Data statistics summary for fluorescence microscopy quantifications

		Analysis from PREM views			
		Value (µm)		Number of data points	
Measurement	*Treatment*	*Mean*	*SEM*	*Filaments*	*Images*
filaments spacing	control	0,184	0,004	50	10
filaments length	control	0,689	0,041	45	6
	myosin S1	1,130	0,045	76	13

Table S2. Data statistics summary for electron microscopy quantifications